Grid nano-indentation as full-field measurements

Y. Gaillard, F. Amiot

FEMTO-ST Institute, CNRS-UMR 6174 / UBFC / ENSMM / UTBM,
24 chemin de l'Épitaphe, F-25030 Besançon, France

Abstract

The use of grid nano-indentation as a full-field measurement tool to investigate the properties of heterogeneous materials is described. Contrarily to the reported approaches which rely on statistical analysis, the mechanical properties fields are analyzed herein relying on a topological description of the sample. The spatial convolution function is approached using Hertz contact theory, and the obtained convolution kernel is used to retrieve the mechanical properties of the different phases. This approach is exemplified on results obtained at very low contact force (and thus very high spatial resolution) on a composite material sample made of micrometer-sized fibers in a polymeric matrix.

Keywords:

Carbon fibres, Elasticity, Mechanical testing, Grid nano-indentation, Full-field measurements, Composites, Graded materials, Interphase

1. Introduction

It is today well known that predicting the global mechanical behavior of composite materials requires more than the mechanical properties of its constituents. Depending on the nature of the phases and on the process-

ing of the composite, the constituents may be either intimately linked (at the crystallographic level) or they can be very poorly linked, for example just by adhesion. Additionally, differences between thermal expansions of the different materials may also lead to fracture at interfaces during the fabrication process, and residual stresses induced by crystallization of a given constituent can dramatically affect the overall properties or result in graded properties [1]. For this kind of materials, the classical mixture law based on the mechanical properties of the constituents is generally not sufficient to fully reproduce the particular macroscopic behavior of the composite itself. The addition of either supplementary phases, whose properties differ from the constituents of the composite, or zones characterized by a gradient of properties is necessary [2, 3]. The experimental characterization of such interfacial phases thus becomes a critical issue [4, 5]. Two strategies can be envisaged to correctly describe the behavior of the composite :

- The first is based on the adjustment of the macroscopic experimental mechanical response, using a model that takes into account this supplementary phase in a representative volume element (RVE) [6, 7]. This strategy is essentially numerical but it requires the knowledge of the mechanical behavior of the phase.

- The second one is the characterization of interfacial mechanical properties, which requires very local characterization methods. These two ways are obviously complementary.

A wide range of local mechanical characterization is now available. Atomic force acoustic microscopy (AFAM) [8] and in particular contact-resonance

atomic force microscopy (CR-AFM) [9] are today rather popular. CR-AFM inherits a very good spatial resolution from the very sharp AFM tip, so that it is a very good choice for who is interested in characterizing interfacial mechanical properties [10, 11]. The quantitative analysis of the measured contact stiffness may however turn to be difficult because of the not so well defined contact geometry (because of the initial tip geometry and because wear usually makes this geometry evolve during the scan) [12]. Alternatively, the very well defined (and calibrated) geometry of indenters makes the investigation of heterogeneous materials by instrumented indentation very promising [13]. The development of high-speed nanoindentation allows to quickly and accurately map the mechanical properties of composite materials with a high spatial resolution and to generate hardness or indentation elastic modulus fields quite easily. Large amount of experimental data are then collected and are to be processed. Classically, the measured properties are analyzed statistically, assuming Gaussian distributions. Each mode in the experimental distribution is thus assumed to correspond to a particular phase [14, 15]. Hardness, elastic modulus, volume fraction of each phase are extracted. The spatial information is then used afterwards to correlate the localization of the different identified phases with their corresponding mechanical properties [16].

The above-cited works actually assume that scale separation apply so that each phase is always probed individually, thus neglecting the interaction between the phases. Homogeneization has thus naturally been introduced in order to analyze nano-indentation data [17, 18]. These two families of approaches thus rely on two extreme assumptions : either one considers

individual phases are probed or one assumes the sole response of the homogeneized composite material is recorded. Probing graded materials, and especially small interfacial regions thus clearly challenges these approaches and requires to relax these assumptions. This is somehow similar to what has been done to analyze nano-indentation results on thin-film materials [19, 20, 21, 22]. This problem has been preferentially addressed using finite-element simulations for two-phase [23, 1] or graded [2] materials, so that interpreting nano-indentation results means a large computation cost. The notable exception is an in-depth sensitivity analysis which has however been conducted in a perturbative framework for very specific inclusion geometries [24].

In the case of fiber/matrix composites, the presence of an interlayer at the interface is strongly suspected but rarely evidenced [3, 25, 26], even though its behavior is critical [27, 28]. Unfortunately, this interlayer is expected to be very thin (less than 1 μm thick) and so, is very difficult to detect and even more to characterize [1, 29, 4, 5]. In this contribution, Polyetherketoneketone (PEKK) reinforced with carbon fibers composite materials has been tested. Samples have been probed perpendicularly to the fibers. Such materials are classically tested by indentation, which allows to clearly distinguish matrix from fibers in terms of hardness and elastic modulus. It will be shown in Sect. 2 that this sample also clearly challenges the statistical approach. In Sect. 3, a method based on a geometrical description of the sample is presented. It assumes the maps obtained by grid nano-indentation result, as for an imaging process, from the convolution of the actual property field with a function depending on the experimental conditions. For the sake of simplicity,

the latter is approached using Hertz contact theory. An influence coefficient based on a priori known informations is defined in order to deconvolve elastic properties of the matrix and the fiber. This method is directly compared to the classical ones. A significant gradient of elastic properties is revealed. The center of the fiber is actually found to be softer than the circumference, and the modulus profile in the matrix close-by the fibers is approached.

2. Grid nano-indentation

This section describes the experimental conditions as well as the statistical analysis of the grid nano-indentation results. The sample consists in a composite material made of PEKK resin together with carbon fibers [30]. These are HexTow AS4 carbon fibers provided by Hexcel as 12000 filament tows, whose longitudinal modulus is about 240 GPa as reported in [31], in line with the manufacturer's specifications [32]. The prepreg has been manufactured using an aqueous impregnation semi-industrial line, with a target volume fraction equal to 55% [33]. Cross section of this sample has been embedded and subsequently polished.

2.1. Nano-indentation measurements

Nanoindentation has been performed using an ultra nanoindenter (UNHT) from Anton Paar. A Berkovich indenter has been used. Indentations are force-controlled. Both loading and unloading rate are set to $120\,\mu\text{N.min}^{-1}$. For this instrument the noise levels have been estimated as $0.05\,\mu$N in force and 0.03 nm in displacement by the manufacturer. $N = 225$ indentations have been performed at $F_m = 60\,\mu$N maximum load (see Fig.1). All the indentations are located on or close by a single carbon fiber, with a nominal

grid spacing equal to 1 μm. The location of the indentations with respect to the fiber has been verified by atomic force microscopy. Indentation hardness and elastic modulus have been extracted using the Oliver and Pharr method [34].

Contact stiffness S at maximum force F_m, and maximum displacement h_m have been extracted from the experimental loading curves. The unloading curve has been fitted using a power law, yielding its exponent m. Using S, F_m, h_m and m, the contact depth h_c has been calculated [34, 35, 36]. The shape of the indenter, giving the tip area calibration as a function of the contact depth $A_c = f(h_c)$, was calibrated using fused silica. It allows to calculate the projected contact area A_c from h_c. Hardness H and the apparent contact modulus E_{eq} are then calculated from

$$H = \frac{F_m}{A_c} \tag{1}$$

$$S = 2E_{eq}\sqrt{\frac{A_c}{\pi}} \tag{2}$$

$$\frac{1}{E_{eq}} = \frac{1-\nu_i^2}{E_i} + \frac{1-\nu^2}{M} \tag{3}$$

This stiffness is hereafter translated into the Young's modulus M of the equivalent isotropic material, assuming that its Poisson's coefficient is $\nu = 0.3$ and considering $E_i = 1141$ GPa and $\nu_i = 0.07$ for the indenter material. For transversely isotropic materials indented orthognally to the isotropy plane, M results from the contribution of 4 of the elastic constants of the material and may be approached using for instance the closed-form expression by Delafargue [37] :

$$\frac{M}{1-\nu^2} = 2\sqrt{\frac{c_{11}c_{33}-c_{13}^2}{c_{11}\left(\frac{1}{c_{44}}+\frac{2}{\sqrt{c_{11}c_{33}}+c_{13}}\right)}} \tag{4}$$

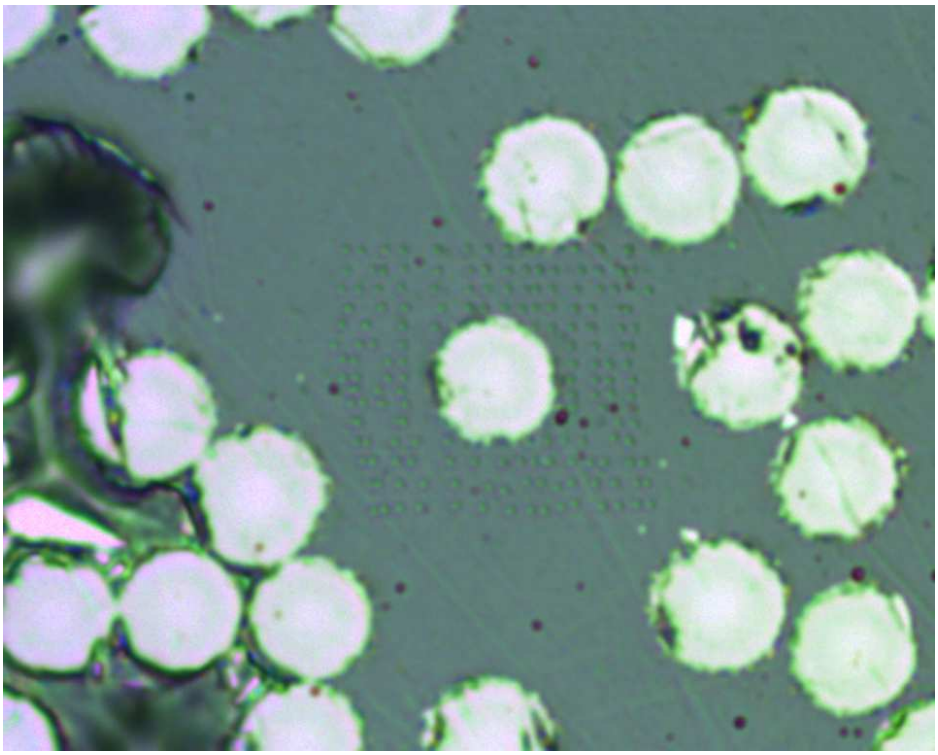

Figure 1: Optical view of the nano-indentation imprints (field of view is $50 \times 40 \mu$m).

, c_{33} being the longitudinal modulus. Using $c_{11} = 10$ GPa, $c_{13} = 36$ GPa, $c_{33} = 240$ GPa and $c_{44} = 10$ GPa yields $M = 54.4$ GPa, thus illustrating the elastic stiffness tensor average performed by nano-indentation measurements. The contact area is also translated in the following in a contact radius $a = \sqrt{\frac{A_c}{\pi}}$.

2.2. Statistical analysis

A statistical analysis of elastic moduli relies on the cumulative density function, $\mathcal{F}(M_c)$ built from the experimental values of elastic moduli $\bar{M}_e$ (e ranging from 1 to N). The properties of the different phases are estimated by assuming a Gaussian distribution of the elastic modulus of each individual

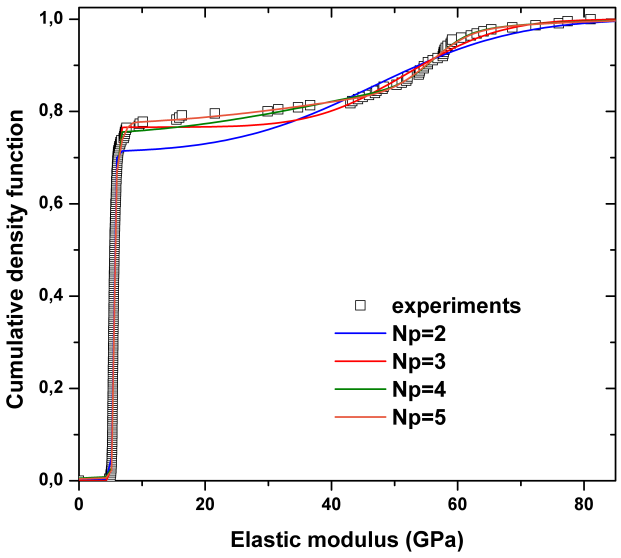

Figure 2: Experimental and estimated cumulated density functions for different N_p values.

phase. The parameters M_n and Δ_{M_n}, describing the modulus of the phase n and the corresponding standard deviation, respectively, are thus estimated by minimizing

$$\eta^2_{cdf} = \sum_{e=1}^{N} \left[\mathcal{F}(\bar{M}_e) - \sum_{n=1}^{N_p} \frac{\omega_n}{2} \left(1 + erf \left(\frac{\bar{M}_e - M_n}{\sqrt{2}\Delta_{M_n}} \right) \right) \right]^2 \tag{5}$$

Figures 2, 3 and 4 display the experimental and estimated cumulated density functions for $2 \leq N_p \leq 7$, and Table 1 shows the corresponding results. Parameters optimization is achieved as described in [38]. The minimum value of the cost function η^2_{cdf} represents the discrepancy between experiment and the calculated cumulative density function. It is presented in Tab. 1, together with the parameters describing the moduli distributions for various N_p values. η^2_{cdf} globally decreases with N_p. However, its values does not

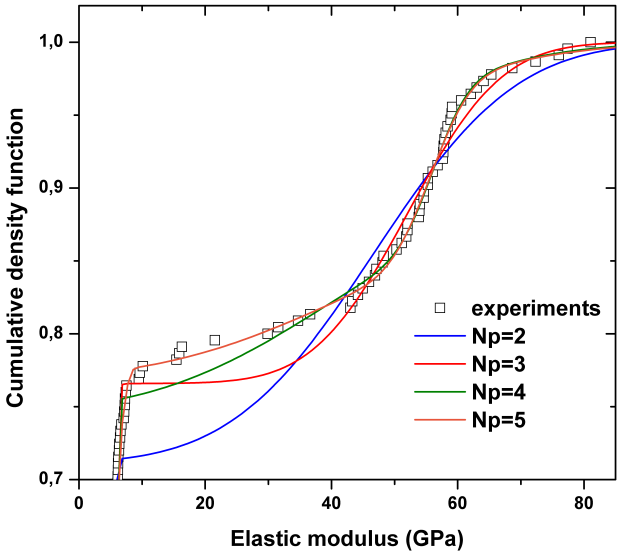

Figure 3: Experimental and estimated cumulated density functions for different N_p values : zoom on the area corresponding to indentations on the fiber.

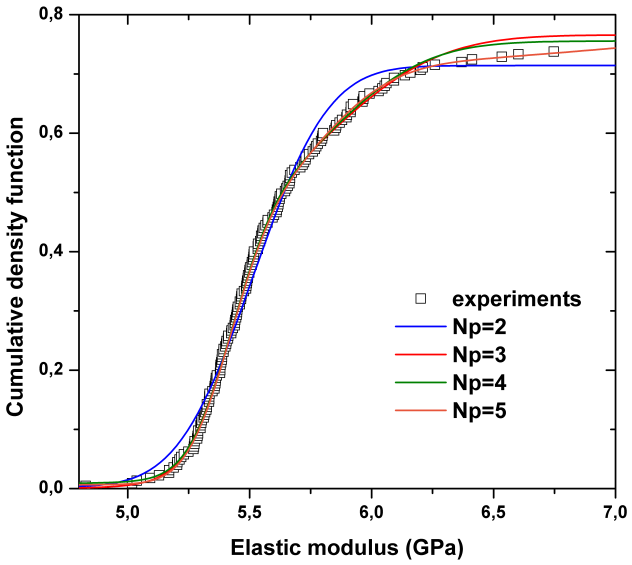

Figure 4: Experimental and estimated cumulated density functions for different N_p values : zoom on the area corresponding to indentations on the matrix.

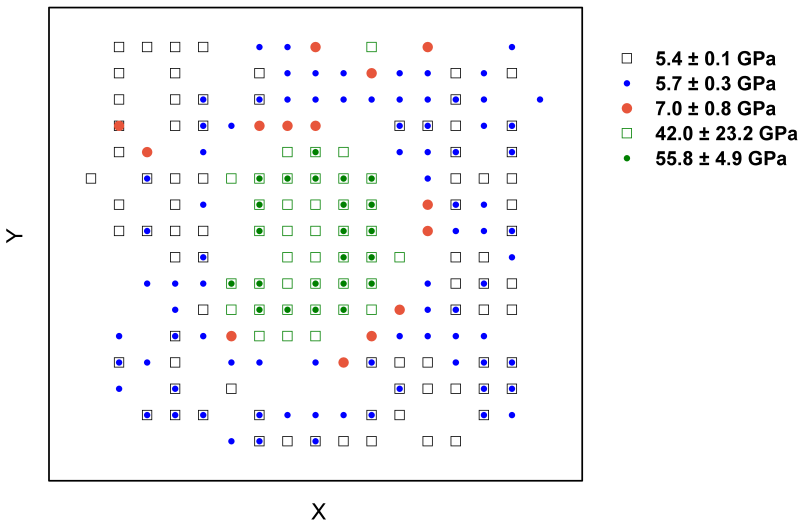

Figure 5: Localization of the indentations belonging to the different phases for $N_p = 5$.

change so much from $N_p = 5$ to $N_p = 7$ thus indicating that the model is over-parametrized for $N_p \geq 5$. Whatever the chosen N_p value, fiber and matrix phases are clearly distinguished.

The resin exhibits an elastic modulus about 5.5 GPa. The distribution corresponding to the fiber appears to be more spread than the one of the matrix. The standard deviation obtained for $N_p = 2$ perfectly illustrates this phenomenon. It provides $\Delta_{M_{matrix}} = 0.2$ GPa and $\Delta_{M_{fiber}} = 17.7$ GPa. Increasing the N_p value makes intermediate value of elastic modulus appear. Focusing on $N_p = 5$, the spatial location of the five modes in the distribution is displayed on Fig.5. It suggests that the center of the fiber is softer than the boundary. It also shows that the properties measured in the region of

Table 1: Elastic moduli identified by statistical analysis as a function of the number of considered populations.

N_p	2	3	4	5	6	7
ω_n	0.71	0.42	0.42	0.41	0.28	0.4
	0.29	0.35	0.33	0.3	0.39	0.31
		0.22	0.15	0.06	0.03	0.05
			0.1	0.11	0.06	0.04
				0.12	0.11	0.12
					0.13	0.06
						0.02
Elastic moduli	5.5 ± 0.24	5.4 ± 0.1	5.4 ± 0.1	5.4 ± 0.1	5.4 ± 0.1	5.4 ± 0.1
(GPa)	46.7 ± 17.7	5.8 ± 0.4	5.8 ± 0.3	5.8 ± 0.3	5.8 ± 0.3	5.8 ± 0.3
		52.1 ± 11.7	39.4 ± 22.1	7 ± 0.8	5.3 ± 0.03	7 ± 0.6
			56.3 ± 4.3	42 ± 23.2	7.1 ± 0.8	11.4 ± 7
				55.8 ± 4.9	44.5 ± 21.2	52.8 ± 14.4
					55.9 ± 4.7	54.5 ± 4.5
						58 ± 0.3
Min η^2_{cdf}	2.9×10^{-6}	3.8×10^{-7}	2.3×10^{-7}	1.1×10^{-7}	1.0×10^{-7}	1.1×10^{-7}

the resin close by the fiber is affected by the presence of the fiber as it could have been expected. It is also clear that the standard deviations associated to the measurements performed inside the fiber are higher than the ones performed in the resin. This mapping together with the value of standard deviation strongly suggest that a gradient of mechanical properties is present inside the fiber. However, such a statistical analysis is unable to describe and characterize more precisely this graded material.

3. Grid nano-indentation data processing

Grid nano-indentation is clearly a way to collect a vast amount of mechanically redundant experimental data. In order to make the most of this redundancy, it is proposed, contrarily to the approach recalled in Sect. 2.2, to make use of some a priori information related to the geometry of the specimen under scrutiny. The convolution kernel translating this geometrical description into the measured indentation moduli map is approached, and the corresponding deconvolution procedure is applied to estimate the elastic properties of the constituents of the sample described in Sect. 2.

3.1. Geometrical description

It is assumed that the probed zone depicted in Fig.1 may be simply described by a two-phases half-space. Namely, the measurement area is assumed to be described by a matrix material in which a single infinite straight fiber whose direction is orthogonal to the indentation plane is included. The full half-space is denoted as $\mathcal{H}$ and the cylinder occupied by the fiber is denoted $\mathcal{C}$.

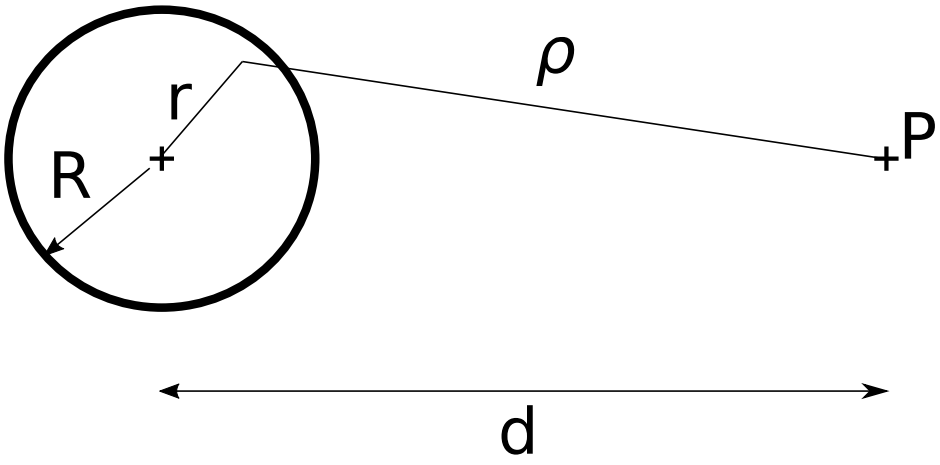

Figure 6: Geometrical description of the sample in the $z = 0$ plane.

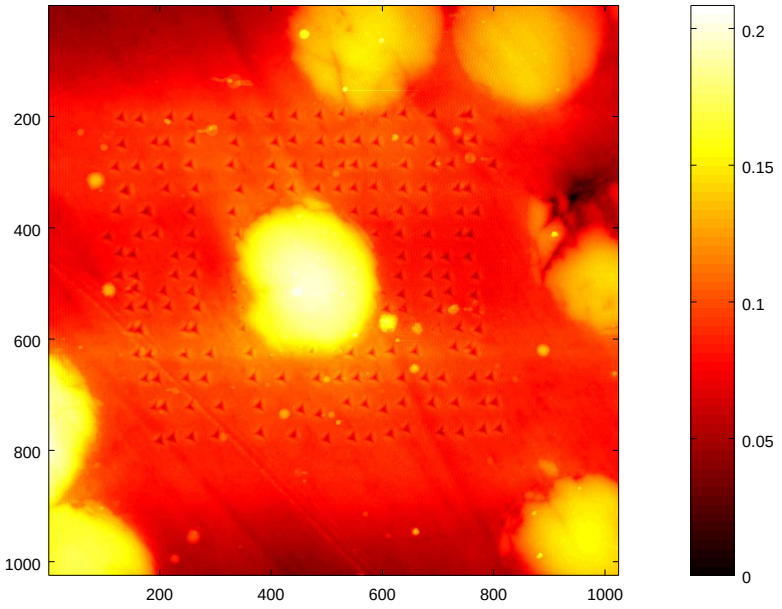

Figure 7: AFM topography of the nano-indentation imprints (μm).

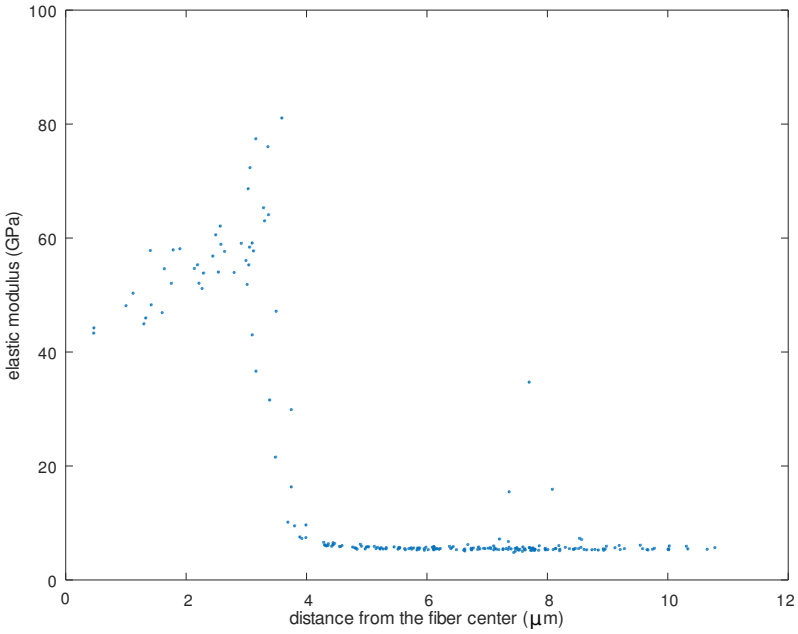

Figure 8: Elastic modulus M_{exp} as a function of the distance to the fiber center.

The problem geometry may thus be described by Fig. 6. The indents positions P, the fiber position and its radius R are obtained by least-square fitting of the AFM topography (acquired after the indentations) presented in Fig. 7, so that all the geometrical parameters in Fig. 6 are experimentally known. In particular, the fiber radius $R = 3.19$ μm and the indents positions are identified. This first allows to display the elastic modulus M_{exp} and the contact radius a as a function of the distance d to the fiber center, owing to the cylindrical symmetry of the problem.

The results are displayed in Fig. 8 and Fig. 9, respectively. These clearly show two different phases, namely a fiber much stiffer and harder than the matrix. It should however be outlined that some outliers may be identified

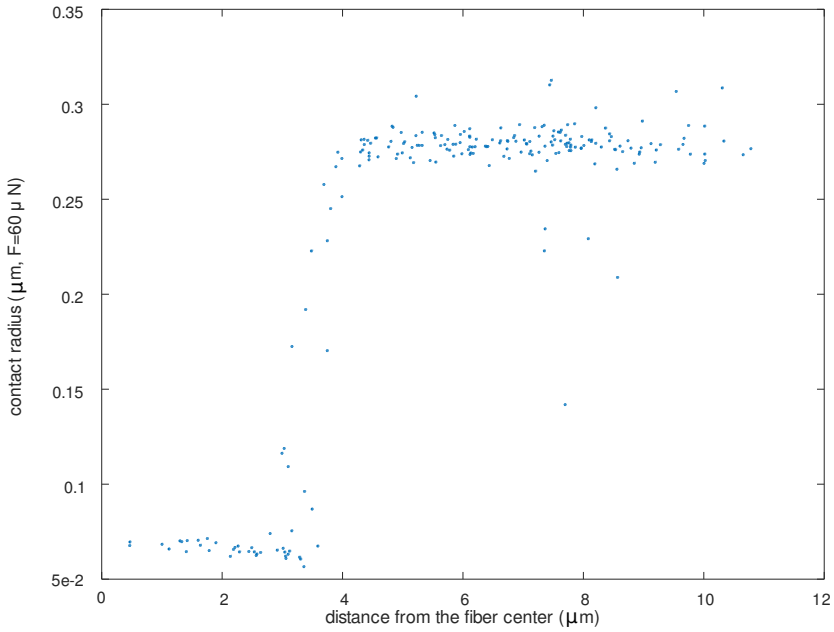

Figure 9: Indentation radius a as a function of the distance to the fiber center.

at $d \simeq 7.5\mu$m. These correspond to indentations performed close by the fiber on top of Fig. 1. The results in Fig. 8 allows to clearly distinguish the matrix and the fiber. An interfacial zone where the measured modulus clearly results from (at least) both the fiber and the matrix is also clearly visible. This convolution effect is sometimes approached by finite-element analysis of the indentation test [1, 39]. The following sections are devoted to a rather different approach. The convolution kernel is approached using analytical expressions and numerical (but straightforward) integration. This very simple computation then allows for the quick estimation of the spatial resolution corresponding to the experimental conditions. The corresponding deconvolution procedure is then applied to retrieve the mechanical properties of the phases.

3.2. Convolution kernel

The contact radius is experimentally determined and corresponds to the loading value at which the material properties are estimated in the standard procedure (see Sect. 2.1) [34]. It is thus assumed that the elastic fields under the indenter may be approached by those deriving from Hertz's contact theory [40], and one restricts herein, for the sake of simplicity, to elastic isotropic materials described by their Young's modulus E and their Poisson's ratio ν. It should then be outlined that the strains ϵ_{ij} scale as

$$\epsilon_{ij} = \frac{3F(1+\nu)}{4\pi E a^3} \epsilon^{\star}_{ij}(a, \nu, \rho, z) \quad \forall i, j \tag{6}$$

and that all the $\epsilon^{\star}_{ij}(a, \nu, \rho, z)$ are known explicitly at any point defined by the cylindrical coordinates (ρ, z) with the origin at P. The reader interested in the detailed expressions may refer to [40] for instance. The scaled strain

energy density $e(a, \nu, \rho, z)$ may thus be computed for any point of the half-space as a function of the $\epsilon^{\star}_{ij}(a, \nu, \rho, z)$.

These fields vanish quickly when moving away from the contact area, highlighting the fact that all points in the half-plane do not equally contribute to the measurement. The key is therefore, for a given geometrical configuration, to approach the contribution of each phase (each point) to the overall measurement. This is very similar to an homogeneization procedure, and as for classical homogeneization, several choices are possible.

It is chosen herein, for the sake of simplicity, to use the fields (6) as test fields. The overall behavior is then obtained by summing the contribution of each phase to the total strain energy. For the geometry depicted in Fig. 6 :

$$M(P)\int_{\mathcal{H}} e(a,\nu,\rho,z)dV = M_{fiber}\int_{\mathcal{C}} e(a,\nu,\rho,z)dV + M_{matrix}\int_{\mathcal{H}\setminus\mathcal{C}} e(a,\nu,\rho,z)dV \tag{7}$$

The scaled strain energy density $e(a, \nu, \rho, z)$ thus acts as a convolution kernel describing the weight of each point in the half-space on the measured indentation modulus. This construction is the equivalent of a Voigt bound in classical homogeneization, and again, any other homogeneization scheme could have been chosen.

Eq. 7 may be recast by defining the influence coefficient $I(\nu, a, P, R)$:

$$I(\nu, a, P, R) = \frac{\int_{\mathcal{C}} e(a,\nu,\rho,z)dV}{\int_{\mathcal{H}} e(a,\nu,\rho,z)dV} \tag{8}$$

The Poisson's ratio is arbitrarily set to $\nu = 0.3$ for both the phases in the following, so that the influence coefficient $I(\nu, a, P, R)$ is computed by standard (Gauss-Kronrod) quadrature. For the considered geometry, the

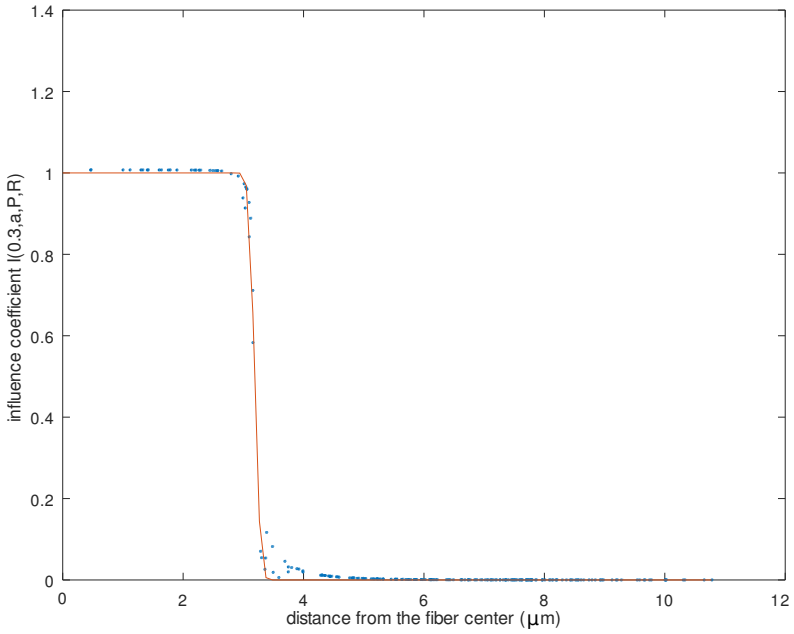

Figure 10: Computed influence coefficient $I(\nu = 0.3, a, P, R)$ as a function of the distance to the fiber center (dots) and the fit by an error function (solid line).

integrations are performed for z ranging from 0 to $10 \times a$ and for ρ also ranging from 0 to $10 \times a$. It is obvious this expression is independent on the probed elastic properties besides the Poisson's ratio.

The obtained values are displayed on Fig. 10 as a function of the distance to the fiber center. It varies from 0 (far from the fiber) to 1 (at the fiber center), and the rather steep change at the matrix/fiber interface suggests that any stiffness gradient at the interface should be resolved. The computed influence coefficient is approached by an error function :

$$I(\nu, a, P, R) \simeq \frac{1}{2} erfc\left(\frac{d(P) - R_f}{\delta}\right) \tag{9}$$

R_f is a fitting parameter, which is adjusted together with δ to approximate the influence function. It allows to estimate the spatial resolution δ in the interface region and the fitting procedure yields $\delta = 190$ nm, thus setting the resolution limit at the interface for this particular set of measurements.

3.3. Deconvolution

Using the influence coefficient defined in Eq. (8) allows one to translate a geometrical description of the sample into the observed indentation modulus field. Under the assumptions defined in Sect. 3.2, the indentation modulus at point P, $M(P)$ reads

$$M(P) = M_{fiber} I(\nu, a, P, R) + M_{matrix}(1 - I(\nu, a, P, R)) \tag{10}$$

This section is devoted to the retrieval of the indentation modulus of each phase from the grid measurements.

3.3.1. Formulation

For any measurement point P, the contact radius $a(P)$ is known as well as the measured indentation modulus $M_{exp}(P)$ (Sect. 3.1). As a consequence, one has one equation 10 for each measurement point P. This large set of linear equations (here : $N = 225$ equations) depends on two parameters, namely M_{fiber} and M_{matrix}. This set of equations may be written

$$\mathcal{M}\mathbf{M}_p = \mathbf{M}_{exp} \tag{11}$$

with

$$\mathcal{M} = \begin{bmatrix} I(\nu, a, P_1, R), & 1 - I(\nu, a, P_1, R) \\ I(\nu, a, P_2, R), & 1 - I(\nu, a, P_2, R) \\ \vdots & \vdots \\ I(\nu, a, P_N, R), & 1 - I(\nu, a, P_N, R) \end{bmatrix} \tag{12}$$

and

$$\begin{aligned} \mathbf{M}_p &= [M_{fiber}, M_{matrix}]^t \\ \mathbf{M}_{exp} &= [M_{exp}(P_1), M_{exp}(P_2), \cdots, M_{exp}(P_N)]^t \end{aligned} \tag{13}$$

The linear system (11) is largely overdetermined and is thus solved in a least-square sense to provide the solution

$$\mathbf{M}_p^s = (\mathcal{M}^t\mathcal{M})^{-1}(\mathcal{M}^t\mathbf{M}_{exp}) \tag{14}$$

together with the residual field $\mathbf{R}$

$$\mathbf{R} = \mathcal{M}\mathbf{M}_p^s - \mathbf{M}_{exp} \tag{15}$$

which is to used to assess the quality of the solution.

3.3.2. Example assuming a uniform fiber

This procedure is applied to the experimental data described in Sect. 3.1. Solving the linear system (11) yields

$$\begin{aligned} M_{fiber} &= 56.1 \text{ GPa} \\ M_{matrix} &= 8.06 \text{ GPa} \end{aligned}$$

and the corresponding residual is displayed in Fig. 11. It should be outlined that most of the residual arises from the fiber, whose indentation modulus seems to display a linear dependence to the radial position. The value for M_{fiber} is however consistent with the reported longitudinal modulus (240 GPa, see Sect. 2.1). One should also highlight that the indentation modulus obtained for the matrix significantly differs from the one obtained by the statistical analysis (see Tab. 1). This indicates that the proposed sample description is not adequate.

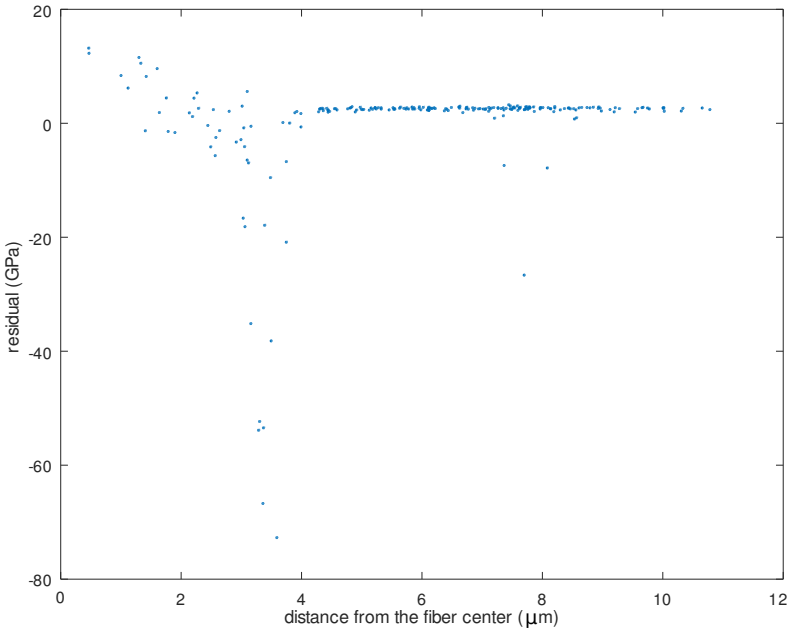

Figure 11: Computed residual assuming a uniform indentation modulus in the fiber.

3.3.3. Example assuming a graded fiber

In order to enrich the description of the sample, one further assumes that the fiber displays a radial gradient of indentation modulus

$$M_{fiber}(r) = M_{center} + (M_{edge} - M_{center})\frac{r}{R} \tag{16}$$

, so that three material parameters are now to be identified. Applying the same procedure yields

$$M(P) = M_{center}I(\nu, a, P, R)+(M_{edge}-M_{center})I_r(\nu, a, P, R)+M_{matrix}(1-I(\nu, a, P, R)) \tag{17}$$

with

$$I_r(\nu, a, P, R) = \frac{\int_{\mathcal{C}} \frac{r}{R} e(a, \nu, \rho, z)dV}{\int_{\mathcal{H}} e(a, \nu, \rho, z)dV} \tag{18}$$

The same deconvolution procedure is applied to yield

$$\begin{aligned} M_{center} &= 37.7 \text{ GPa} \\ M_{edge} &= 64.7 \text{ GPa} \\ M_{matrix} &= 7.99 \text{ GPa} \end{aligned}$$

thus outlining the significant modulus gradient in the fiber, which is very similar to the results obtained in [1] by the use of extensive finite-element simulations for similar fibers. Such a modulus gradient is also observed by other local characterization techniques [41].

The corresponding residual is also displayed in Fig. 12. It clearly shows that most of the residual now comes from the matrix region right next to the fiber. Again, the indentation modulus obtained for the matrix differs from the value obtained by the statistical analysis. This further calls for a better description of the sample out of the fiber.

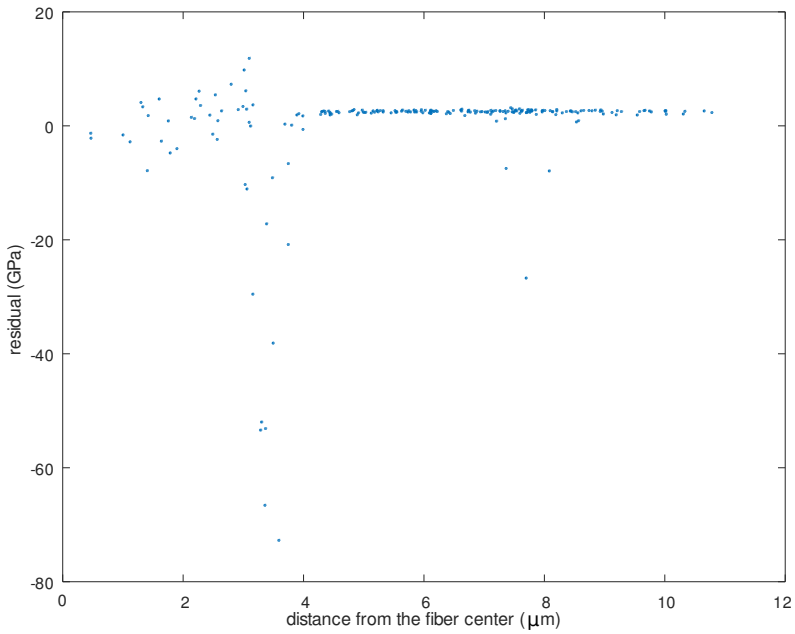

Figure 12: Computed residual assuming a radial distribution for the indentation modulus in the fiber.

3.3.4. Example assuming graded fiber and matrix

In order to enrich the description of the sample, one further assumes that the matrix displays a radial gradient of indentation modulus below a cut-off radius $R_I = 4\mu$m. Its modulus now reads

$$\begin{aligned} M_{matrix}(r) &= \frac{M_{bulk}R - M_I R_I}{R - R_I} + (M_I - M_{bulk})\frac{r}{R - R_I} \text{ if } R \leq r \leq R_I \\ M_{matrix}(r) &= M_{bulk} \text{ if } r \geq R_I \end{aligned}$$

, so that four material parameters are now to be identified. Applying the same procedure yields

$$\begin{aligned} M(P) &= M_{center}I(\nu, a, P, R) + (M_{edge} - M_{center})I_r(\nu, a, P, R) + M_{bulk}(1 - I(\nu, a, P, R)) \\ &+ \frac{R_I(M_{bulk} - M_I)}{R - R_I}\left(I(\nu, a, P, R_I) - I(\nu, a, P, R)\right) \\ &+ \frac{M_I - M_{bulk}}{R - R_I}\left(R_I I_r(\nu, a, P, R_I) - R I_r(\nu, a, P, R)\right) \end{aligned} \quad (19)$$

The deconvolution procedure then yields

$$\begin{aligned} M_{center} &= 42.7 \text{ GPa} \\ M_{edge} &= 59.0 \text{ GPa} \\ M_{bulk} &= 5.4 \text{ GPa} \\ M_I &= 71.2 \text{ GPa} \end{aligned}$$

The corresponding residual is also displayed in Fig. 13. It clearly shows that adding a linear dependence of the matrix modulus close by the interface significantly improves the overall residual, thereby proving a much better description of the sample properties. It should be outlined that the residual

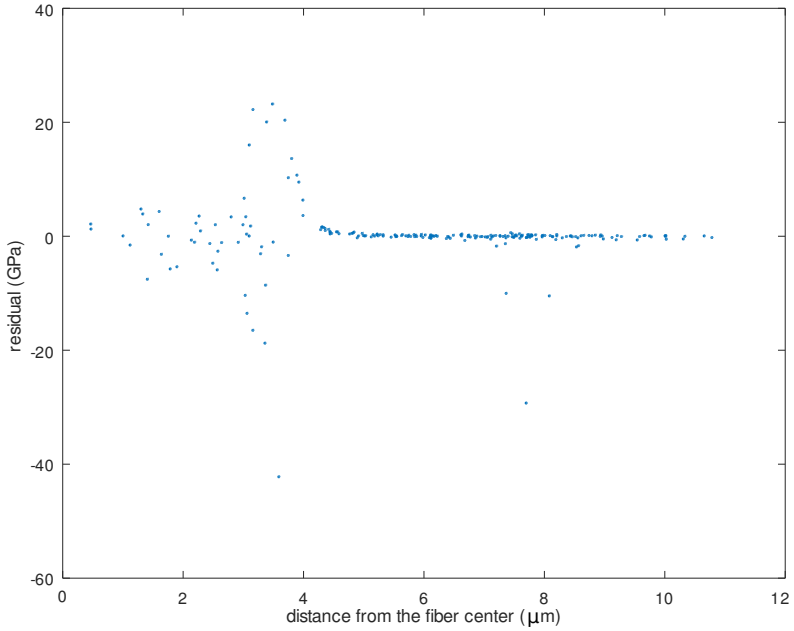

Figure 13: Computed residual assuming a radial distribution for the indentation modulus in the fiber and a radial gradient of the indentation modulus in the matrix up to a distance $R_I = 4\mu$m.

is now almost 0 in the matrix far from the fiber, contrarily to the previous modelings (see Figs. 11 and 12). The remaining residual in Fig.13 also suggests that a more complex modulus distribution in the matrix close-by the fiber is to be identified. This approach by successive enrichment of the sample description clearly reveals, at least qualitatively, the presence of a very steep modulus gradient in a ring which is about 800 nm thick around the fiber. This is made possible by considering the data collected in grid nano-indentation as field information and processing these as they result from an imaging process : adding some a priori information on the sample description allows one to deconvolve the measured data and reveal features whose size approaches the resolution of the imaging process.

The residual may be further analyzed with Fig. 14, which has been obtained by combining :

- The normalized topography $\frac{z(x,y)}{\max|z(x,y)|}$
- The normalized residual $\frac{|R(x,y)|}{\max|R(x,y)|}$ obtained by linear interpolation from the measurement points where it is available, outside the graded ring.

This figure therefore allows to localize areas where the proposed modeling is not adequate and to compare these with topographic features. It can be seen from this figure, and also by comparing to the topography displayed in Fig. 7, that the residual is not spatially correlated to scratches or defects. It is mainly dominated by the presence of a second fiber, which affects the measured moduli but is not taken into account in the analysis. This allows us to conclude that these defects do not significantly affect the values in

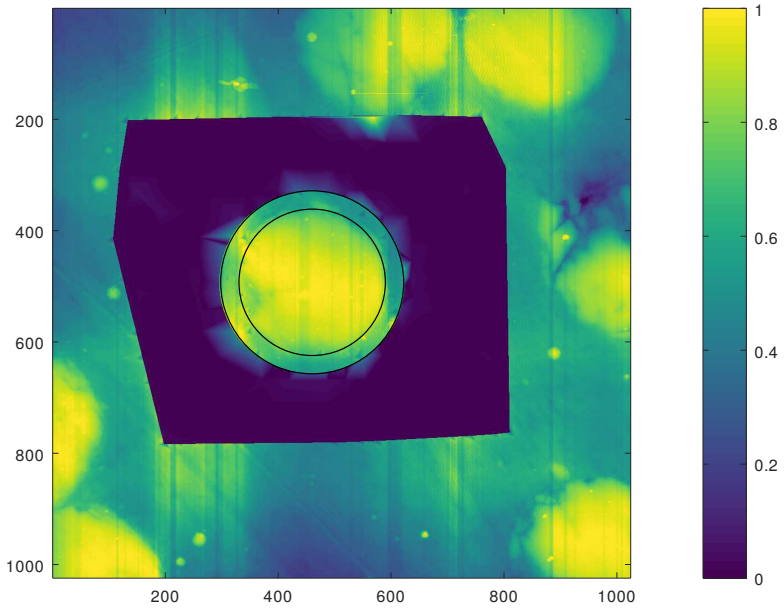

Figure 14: Composite view for the comparison of the defects position with the residual distribution. The two circles correspond to the limit of the fiber and to the outer limit of the ring of matrix with a graded stiffness.

the matrix. This also highlights how the residual can (and should) be used together with material knowledge to drive any modeling enrichment.
Finally, the robustness of the proposed approach may be further illustrated by comparing the indentation modulus obtained for the matrix with the proposed method ($M_{bulk} = 5.4$ GPa) with the value obtained by statistical analysis (5.4 ± 0.1 GPa for $N_p > 2$ in Sect. 2.2). This agreement validates the proposed description. Results obtained in the bulk matrix further illustrate how making use of the geometrical description regularize the final properties. These geometrical assumptions are strong assumptions : the indentation modulus is for example imposed to be uniform in the matrix phase (outside the graded ring), so that the effect of few local defects would be smeared out in the final results. This is thought to be the origin of the robustness of the proposed method. Should these assumptions be inadequate (because of heterogeneities resulting from scratches or polishing defects), the residual field should be affected.

4. Conclusions

It is proposed herein the use of grid nano-indentation as a full-field measurement tool to investigate the properties of heterogeneous samples, relying on a geometrical description of the sample. The spatial convolution function is approached using Hertz theory, and the obtained convolution kernel is used to retrieve the mechanical properties of the different phases of a composite material sample made of micrometer-sized fibers in a polymeric matrix. It particularly allows to approach the structure of the sample at the finer scale, and revealed herein a very steep modulus gradient for the matrix material

in a thin ring around the fiber. Such a description could be obtained by a successive enrichment, which is driven by the residual of the projection onto the convolution kernel. This analysis method is thus expected to provide some useful insight into interfacial regions of composite materials.

Acknowledgments

Saber Chelaghma (IRT St-Exupéry) and Jean-Noël Périé (Institut Clément Ader) are gratefully acknowledged for providing the material sample used in this study.

References

[1] Cole D.P., Henry T.C., Gardea F., Haynes R.A. (2017) Interphase mechanical behavior of carbon fiber reinforced polymer exposed to cyclic loading. Composites Sciences and Technology 151:202-210.

[2] Armitage O.E., Oyen M.L. (2017) Indentation across interfaces between stiff and compliant tissues. Acta Biomaterialia 56:36-43.

[3] Chevalier J., Camanho P.P., Lani F., Pardoen T. (2019) Multi-scale characterization and modelling of the transverse compression response of unidirectional carbon fiber reinforced epoxy. Composite structure 209:160.

[4] Perrier A., Le Bourhis E., Touchard F., Chocinski-Arnault L. (2016) Effect of water ageing on nanoindentation response of single hemp yarn/epoxy composites. Composites: Part A 84:216-223.

[5] Enrique-Jimenez P., Quiles-Dias S., Salavagione H.J., Fernadez-Blazquez J.P., Monclus M.A., Guzman de Villoria R., Gomez-Fatou M.A., Ania F., Flores A. (2019) Nanoindentation mapping of multiscale composites of graphene-reinforced polypropylene and carbon fibres. Composites Sciences and Technology 169:151-157.

[6] Panamoottil S.M., Das R., Jayaraman K. (2017) Towards a multiscale model for flax composites from behaviour of fibre and fibre/polymer interface. Journal of Composite Materials 51:859-873

[7] Zhong Y., Tran L.Q.N., Kureemun U., Lee H.P. (2017) Prediction of the mechanical behavior of flax polypropylene composites based on multi-scale finite element analysis. Journal of Materials Science 52:4957.

[8] Rabe U. (2006) Atomic force acoustic microscopy, in : Applied scanning probe methods, vol II. Berlin, Springer-Verlag, 37-90.

[9] Hurley D.C. (2009) Contact resonance force microscopy techniques for nanomechanical measurements, in : Applied scanning probe methods, vol XI. Berlin, Springer-Verlag, 97-138.

[10] Nair S.S., Wang S., Hurley D.C. (2010) Nanoscale characterization of natural fibers and their composites using contact-resonance force microscopy. Composites: Part A 41:624-631.

[11] Nair S.S., Hurley D.C., Wang S., Young T.M. (2013) Nanoscale characterization of interphase properties in maleated polypropylene-treated natural fiber-reinforced polymer composites. Polym. Eng. Sci. 53:888-896.

[12] Arnould O., Arinero R. (2015) Towards a better understanding of wood cell wall characterisation with contact resonance atomic force microscopy. Composites: Part A 74:69-76.

[13] Gibson R.F. (2014) A review of recent research on nanoindentation of polymer composites and their constituents. Composites Sciences and Technology 105: 51-65.

[14] Constantinides G.. Ravi Chandran K.S., Ulm F.J., Van Vliet K.J. (2006) Grid indentation amalysis of composite microstructure and mechanics: principles and validation. Materials Science and Engineering A 430: 198-202.

[15] Ulm F.J., Vandamme M., Bobko C., Alberto Ortega J., Tai K., Ortiz C. (2007) Statistical Indentation Techniques for Hydrated Nanocomposites: Concrete, Bone, and Shale. J. Am. Ceram. Soc. 90:2677.

[16] Tromas C., Arnoux M., Milhet X. (2012) Hardness cartography to increase the nanoindentation resolution in heterogeneous materials: Application to a Ni-based single-crystal superalloy. Scripta Mater 66:77-80.

[17] Randall N.X., Vandamme M., Ulm F.J. (2008) Nanoindentation analysis as two-dimensional tool for mapping the mechanical properties of complex surfaces. J. Mater. Res. 24(3):679-690.

[18] Argatov I.A., Sabina F.J. (2017) A two-phase self-consistent model for the grid indentation testing of composite materials. International Journal of Engineering Science 121:52-59.

[19] Bec S., Tonck A., Loubet J.L. (2006) A simple guide to determine elastic properties of films on substrate from nanoindentation experiments. Phil. Mag. 86:5347.

[20] Jäger I.L. (2002) Comment on: Effects of the substrate on the determination of thin films mechanical properties by nanoindentation by Saha and Nix. Scripta Mater. 47:429.

[21] Saha R., Nix W.D. (2002) Effects of the substrate on the determination of thin film mechanical properties by nanoindentation. Acta Mater. 50:23.

[22] Perriot A., Barthel E. (2004) Elastic contact to a coated half-space. Effective elastic modulus and real penetration. J. Mater. Res. 19:600.

[23] Durst K., Göken M., Vehoff H. (2004) Finite element study for nanoindentation measurements on two-phase materials. J. Mater. Res. 19:85.

[24] Argatov I.I., Sabina F.J. (2020) Contact stiffness indentation tomography: moduli-perturbation approach. International Journal of Engineering Science 146:103175.

[25] Ureña A., Rams J., Escalera M.D., Sánchez M. (2005) Characterization of interfacial mechanical properties in carbon fiber/aluminium matrix composites by the nanoindentation technique. Composites Sciences and Technology 65: 2025-2038.

[26] Diez-Pascual A.M., Gomez-Fatou M.A., Ania F., Flores A. (2012) Nanoindentation assessment of the interphase in carbon nanotube-based hierarchical composites. J. Phys. Chem C 116(45):193-200.

[27] Liu Z., Zhao F., Jones F.R. (2008) Optimising the interfacial response of glass fibre composites with a functional nanoscale plasma polymer coating. Composites Sciences and Technology 68: 3161-3170.

[28] Hodzic A., Kim J.K., Lowe A.E., Stachurski Z.H. (2004) The effects of water aging on the interphase region and interlaminar fracture toughness in polymer-glass composites. Composites Sciences and Technology 64: 2185-2195.

[29] Hausild P., Cech J., Materna A., Matejicek J. (2019) Statistical treatment of grid indentation considering the effect of the interface and the microstructural length scale. Mechanics of Materials 129:99-103.

[30] Chelaghma S., DeAlmeida O., Margueres P., Perie J.-N., Passieux J.-C., Vinet A. (2018) Characterization of multifunctional composite materials. JEC Composites magazine 125:62-65.

[31] Herráez M., Fernández A., González C., Lopes C.S. (2016) Strength and toughness of structural fibres for composite material reinforcement. Philosophical Transactions of the Royal Society A: Mathematical, Physical and Engineering Sciences 374.

[32] https://www.hexcel.com/user_area/content_media/raw/AS4_HexTow_DataSheet.pdf

[33] https://www.irt-saintexupery.com/wp-content/uploads/2017/03/Impregnation_line_

[34] Oliver, W.C. and Pharr, G.M. (1992) An Improved Technique for Determining Hardness and Elastic Modulus Using Load and Displacement Sensing Indentation Experiments. J. Mater. Res. 7:1564-1583.

[35] Woirgard J., Dargenton J-C. (1997) An alternative method for penetration depth determination in nanoindentation measurements. J. Mater. Res. 12:2455.

[36] Oliver W.C., Pharr G.M. (2004) Measurement of Hardness and Elastic Modulus by Instrumented Indentation: Advances in Understanding and Refinements to Methodology. J. Mater. Res 19:3-20.

[37] Delafargue A., Ulm F.-J. (2004) Explicit approximations of the indentation modulus of elastically orthotropic solids for conical indenters. Int. Jal. Solids Struct. 41(26): 7351-7360.

[38] Qasmi M., Delobelle P., Richard F., Brun C., Fromm M. (2006) Viscoelastic mechanical properties determined by nanoindentation tests and its numerical modelling of polypropylene modified by He+ particle implantation and e irradiation. Progress in organic coatings 51 (3):195-204.

[39] Lee S.-H., Wang S., Pharr G.M., Xu H. (2007) Evaluation of interphase properties in a cellulose fiber-reinforced poltpropylene composite by nanoindentation and finite element analysis. Composites: Part A 38:1517-1524.

[40] Hanson M.T., Johnson T. (1993) The elastic field for spherical Hertzian contact of isotropic bodies revisited : some alternative expressions. Jal Tribology 115:327.

[41] Gu Y., Li M., Wang J., Zhang Z. (2010) Characterization of the interphase in carbon fiber/polymer composites using a nanoscale dynamic mechanical imaging technique. Carbon 48:3229-3235.